

A Dual Tissue-Doppler Optical-Flow Method for Speckle Tracking Echocardiography at High Frame Rate

Jonathan Porée^{ID}, Mathilde Baudet, François Tournoux, Guy Cloutier, and Damien Garcia^{ID}

Abstract—A coupled computational method for recovering tissue velocity vector fields from high-frame-rate echocardiography is described. Conventional transthoracic echocardiography provides limited temporal resolution, which may prevent accurate estimation of the 2-D myocardial velocity field dynamics. High-frame-rate compound echocardiography using diverging waves with integrated motion compensation has been shown to provide concurrent high-resolution B-mode and tissue Doppler imaging (TDI). In this paper, we propose a regularized least-squares method to provide accurate myocardial velocities at high frame rates. The velocity vector field was formulated as the minimizer of a cost function that is a weighted sum of: 1) the ℓ^2 -norm of the material derivative of the B-mode images (optical flow); 2) the ℓ^2 -norm of the tissue-Doppler residuals; and 3) a quadratic regularizer that imposes spatial smoothness and well-posedness. A finite difference discretization of the continuous problem was adopted, leading to a sparse linear system. The proposed framework was validated *in vitro* on a rotating disk with speeds up to 20 cm/s, and compared with speckle tracking echocardiography (STE) by block matching. It was also validated *in vivo* against TDI and STE in a cross-validation strategy involving parasternal long axis and apical three-chamber views. The proposed method based on the combination of optical flow and tissue Doppler led to more accurate time-resolved velocity vector fields.

Index Terms—High-frame-rate echocardiography, velocity vector imaging, speckle tracking echocardiography, diverging waves, tissue Doppler imaging, optical flow.

I. INTRODUCTION

GIVEN its non-invasive nature and extensive availability, transthoracic echocardiography (TTE) is the most widely used imaging modality to evaluate myocardial dysfunction [1]. In TTE, the evaluation of regional myocardial function is usually performed using either Doppler methods or speckle tracking echocardiography (STE). Pulse-wave Doppler provides accurate measurements of myocardial wall velocities with high temporal resolution (~ 500 scanlines/s), but this single-range acquisition process is restricted to regional measurements. Using sequential line-by-line scanning, tissue Doppler imaging (TDI) evaluates velocities in the entire field of view. There is however a trade-off between the frame rate and the spatial resolution (*i.e.*, line density), which may prevent the accurate derivation of tissue strains and strain rates [2]. Furthermore, unless multiple coplanar acquisitions are combined, as in [3], Doppler is unable to provide multi-component velocities (2-D or 3-D). As an alternative, by following the speckle patterns in a series of B-mode sequences, speckle-tracking echocardiography has the ability to overcome the one-dimensionality limitation of TDI. To be efficient, STE requires high-contrast and high-resolution B-mode images. In conventional ultrasound systems, this may be achieved by increasing the image line density, but at the expense of the frame rate. Although STE is able to quantify local motion within the myocardium in resting patients [4], the limited frame rate may become an issue during stress echocardiography [5] when the heart rate is increased to modify the myocardial dynamics. Multi-dimensional motion estimation also remains a challenge in echocardiography because of the limited cross-range resolution (*i.e.*, perpendicular to the direction of the beam) of phased array transducers. Different methods have been proposed to address the problem of 2-D velocity estimation within the myocardium [3], [6]–[9]. Sühling *et al.* [6], [7] applied a multi-scale optical flow approach on B-mode echocardiograms to retrieve 2-D velocity vector fields. At conventional frame rates, optical flow methods can be sensitive to intensity variations associated with large frame-to-frame or out-of-plane motions. Although TDI provides in-range velocities only, they are less sensitive

Manuscript received January 18, 2018; accepted February 23, 2018. Date of publication March 2, 2018; date of current version August 30, 2018. This work was supported in part by the Natural Sciences and Engineering Research Council of Canada under Grant RGPAS-477914-2015 and Grant RGPIN-04217-2015, in part by the Fonds de Recherche du Québec—Nature et Technologies under Grant 2016-PR-189822, in part by the Collaborative Health Research Program of the Natural Sciences and Engineering Research Council of Canada under Grant CHRP 462240-14, and in part by the CIHR under Grant CPG-134748. (Corresponding author: Jonathan Porée.)

J. Porée was with the Laboratory of Biorheology and Medical Ultrasonics, Research Center, University of Montreal Hospital, Montreal, QC H2X 0A9, Canada (e-mail: jonathan.poree@gmail.com).

M. Baudet and F. Tournoux are with the Department of Echocardiography, University of Montreal Hospital, Montreal, QC H2L 4M1, Canada.

G. Cloutier is with the Laboratory of Biorheology and Medical Ultrasonics, Research Center, University of Montreal Hospital, Montreal, QC H2X 0A9, Canada, and also with the Department of Radiology, Radio-Oncology and Nuclear Medicine, Institute of Biomedical Engineering, University of Montreal, Montreal, QC H3C 3J7, Canada.

D. Garcia was with the Department of Radiology, Radio-Oncology and Nuclear Medicine, Institute of Biomedical Engineering, University of Montreal, Montreal, QC H3C 3J7, Canada. He is now with Univ Lyon, INSA-Lyon, CREATIS, UMR5220, U1206, 69621 Lyon, France.

Color versions of one or more of the figures in this paper are available online at <http://ieeexplore.ieee.org>.

Digital Object Identifier 10.1109/TMI.2018.2811483

to intensity variations than optical flow methods [10], [11]. Arigovindan *et al.* [3] thus introduced a regularized cross-beam vector Doppler method to retrieve planar myocardial motion. This method remains limited in clinical echocardiography since it requires registering at least two successive acquisitions, with different angular positions. To improve the performance of B-mode optical flow methods, Porrás *et al.* [8] and Tavakoli *et al.* [9] recently proposed its combination with tissue Doppler imaging by exploiting interleaved B-mode and TDI sequences. Nevertheless, using conventional ultrasound imaging, duplex sequences are limited by their relatively low frame rate (~ 30 frames/s). Recent developments in ultrasound imaging using either multi-line transmits [12], [13], synthetic apertures [14], compounded plane waves [15]–[18] or compounded diverging waves [19]–[22] allow one to reach very high frame rates (hundreds of frames per second) and ubiquitously focused images through dynamic focusing and coherent compounding [15]. Assessment of the myocardial dynamics by speckle tracking is possible only if the speckle patterns are well preserved. In echocardiography, however, the rapid motion of the myocardium may alter coherent summation. Indeed, tissue motion, if ignored, induces phase delays that might alter the speckles due to destructive interferences. Andersen *et al.* [41] have addressed this problem at high frame rates (500 frames per second - FPS) by using a parallel receive beamformer (“explososcanning”, [23]) to obtain long-axis views of the left ventricle. To deal with the relatively poor contrast of their images (no coherent compounding was used), they introduced a multi-step tracking method including: spatial and temporal filtering, detection of high-intensity speckles, constrained feature tracking, and final smoothing. In this original feasibility study, they tested their approach in ten subjects and confirmed that speckle tracking is possible in high-frame-rate echocardiography. Using compound schemes, high-resolution imaging of rapidly moving tissues can be achieved through motion compensation [17], [24]–[26]. In a recent study [19], we proposed an effective design for motion compensation (MoCo) in high-frame-rate echocardiography with wide diverging waves. This method uses a modified autocorrelation method to evaluate the tissue Doppler velocities during transmission, and compensates for the motion-induced phase delays during coherent compounding. At the opposite of state-of-the-art echocardiography methods, this original sequence was able to provide both B-mode and TDI in wide-field sectors at a much higher frame rate (~ 250 FPS) than conventional line-by-line sequences (limited to ~ 50 FPS). This approach could overcome the limitation of dual TDI / optical-flow methods [8], [9], [27].

In the present study, we introduce a regularization method to reconstruct 2-D myocardial velocity vector fields in high-frame-rate echocardiography. Taking advantage of the duplex nature of the high-frame-rate echocardiography method we developed [19], TDI and B-mode were combined in a regularized least-squares approach by minimizing a quadratic cost function defined as the weighted sum of: 1) the ℓ^2 -norm of the material derivative of the B-mode images (optical flow) to evaluate the 2-D velocity field, 2) the ℓ^2 -norm of the tissue-Doppler residuals to increase in-range accuracy, and

3) a quadratic regularizer that imposes spatial smoothness on the velocity vector field. We compared the proposed global method against block matching by 2-D cross-correlation in an *in vitro* phantom. The algorithm was also validated *in vivo* in five healthy volunteers using a cross-validation strategy (*i.e.*, comparison between the apical 3-chamber (A3C) and the parasternal long-axis (PSLA) view vector field).

II. ULTRAFAST ECHOCARDIOGRAPHY

In this section, we briefly recall the principles of the ultrafast duplex (*i.e.*, B-mode and TDI) echocardiography sequence with integrated motion compensation [19].

A. Motion Compensation & Coherent Compounding

To produce high-contrast and high-resolution images of the myocardium, successive diverging beams with different tilted angles were transmitted and the echoes were compounded coherently. To ensure the coherent summation of the received analytic signals, we adopted the motion compensation method introduced in our previous study [19]. In this method, N_{TX} tilted transmit angles are organized in a triangular sequence (see [19, Fig. 3]). This specific arrangement, along with Doppler-based MoCo, ensures the coherent summation of the main lobes, while side-lobes are summed incoherently (see [19, Fig. 4]). The measured tissue phase shifts ϕ_{MoCo} are used to compensate for relative tissue motion before coherent compounding. High-frame-rate TDI can be deduced using:

$$v_D = \frac{PRF}{4\pi f_0} c \phi_{\text{MoCo}}, \quad (1)$$

where v_D is the tissue Doppler velocity, PRF the pulse repetition frequency, c the speed of sound, and f_0 the central frequency of the probe. In the present study, tissue Doppler standard deviation (σ_D) was also evaluated to provide information on TDI precision and MoCo efficiency (as it depends on ϕ_{MoCo}). It was computed as follows:

$$\sigma_D = \frac{PRF}{4\pi f_0 (N_{TX} - 1)} \sqrt{\sum_{n=1}^{N_{TX}-1} \left(\angle \widetilde{s}_n \widetilde{s}_{n+1} - \phi_{\text{MoCo}} \right)^2}. \quad (2)$$

Here \widetilde{s}_n is the complex envelope image corresponding to the n -th transmitted diverging beam (see bottom left panel in Figure 1). This parameter was used to weight the contribution of the Doppler and optical flow constraints (see Section III.A.4.)

B. Transmit Sequence

To produce high-frame-rate echocardiographic images of the myocardium, series of $N_{TX} = 36$ successive tilted diverging beams (width: 90° , tilt: -16° to 16°) were transmitted using a Philips/ATL P4-2 phased array transducer (64 elements, central frequency $f_0 = 2.5$ MHz, pitch = 0.3 mm). The pulse repetition frequency was set to 4500 Hz for a maximum acquisition depth of 15 cm. The analytic signals were beamformed [28] to get the compound complex envelopes. Motion compensation was integrated in the compounding

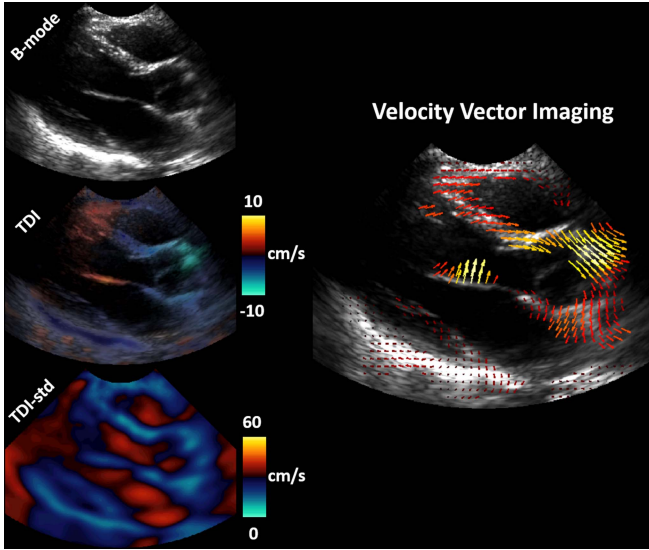


Fig. 1. High-frame rate echocardiography for tissue velocity vector imaging (VVI). Motion compensated beamforming [19] was used to generate the input data (B-mode, tissue Doppler and tissue-Doppler standard deviation) at 500 frames/s. These data were combined in a regularized problem to provide a robust VVI method.

process [19] using a 75% time-overlap sliding window to provide high-resolution B-mode, TDI and TDI-standard deviation at 500 FPS (*i.e.*, frame rate = $\frac{PRF}{N_{TX} \times (1-75\%)} = \frac{4500}{36 \times (1-75\%)} = 50$ Hz).

III. MATHEMATICAL FRAMEWORK

In this section, we describe the proposed Velocity Vector Imaging (VVI) framework. Let $\vec{v} = \{v_x, v_z\}$ be the 2-D velocity field discretized in a Cartesian grid whose coordinates are $\{x, z\}$. Our aim was to recover the tissue velocity \vec{v} from the measurement set $\{I, v_D, \sigma_D\}$ provided by ultrafast echocardiography [19], where $I = |IQ|^{0.5}$ refers to the gamma-compressed envelope images. We first describe the regularization scheme in the continuous domain.

A. Spatial Representation of the Functional

The proposed regularized least-squares problem is an extension of the classical Horn-Schunck algorithm [29], [30] adapted for high-frame-rate echocardiography. It consists in a weighted sum of three terms: 1) a B-mode optical flow, 2) a tissue-Doppler-based residual norm and 3) a vector regularizer, as now detailed.

1) *Optical Flow*: Let Ω be the domain of interest, a closed region which includes the myocardium. The optical flow functional involves the constancy of local brightness while tissue moves inside the field of view. It is defined as:

$$J_{\text{of}}(\vec{v}) = \int_{\Omega} \omega_{\text{of}} \left(\vec{d}_{\text{of}} \cdot \vec{v} - v_{\text{of}} \right)^2 \quad (3)$$

where ω_{of} is a pixelwise weight function for the optical flow constraint (see Section III.A.4, “Robust regularization using reweighted least squares”), $\vec{d}_{\text{of}} = \vec{\nabla}I / \|\vec{\nabla}I\|$ is the normalized image gradient vector giving the local orientation of the B-mode texture, and $v_{\text{of}} = -\partial_t I / \|\vec{\nabla}I\|$ is the apparent texture

velocity along \vec{d}_{of} . The normalization by $\|\vec{\nabla}I\|$ ensures that the overall functional is dimensionally homogeneous to a squared velocity. To prevent outliers in regions where image gradient is small (*i.e.*, where v_{of} might diverge), ω_{of} was set to 0 when $|v_{\text{of}}| > V_N$ ($V_N = \text{Nyquist Doppler velocity}$).

2) *Tissue Doppler*: The second term of the cost function is a tissue Doppler constraint defined as:

$$J_D(\vec{v}) = \int_{\Omega} \omega_D \left(\vec{d}_D \cdot \vec{v} - v_D \right)^2, \quad (4)$$

where ω_D is the corresponding pixelwise weight function (see Section III.A.4, “Robust regularization using reweighted least squares”), \vec{d}_D is a unitary vector describing the Doppler direction, and v_D is the tissue Doppler velocity given by the ultrasound MoCo sequence (see Eq. 1). The relative contribution of the optical flow and TDI constraints was adjusted through the constant parameter $p \in [0, 1]$:

$$J_{\text{Data}}(\vec{v}) = (1-p)J_{\text{of}}(\vec{v}) + pJ_D(\vec{v}). \quad (5)$$

3) *Vector Regularization*: If it exists a location where \vec{d}_D and \vec{d}_{of} are equal, the problem is ill-posed and the solution is not unique. If the vectors \vec{d}_D and \vec{d}_{of} are different for any location, the problem is well-posed and minimizing J_{Data} results in an invertible system. In practice, some \vec{d}_D and \vec{d}_{of} are approximately equal so that the problem is ill-conditioned. Another constraint is required to make the algorithm stable; a regularization term was thus added to (5). We used a second order regularizer similar to that proposed by Corpetti *et al.* [31], based on the divergence and curl of the velocity field:

$$\begin{aligned} \text{div}(\vec{v}) &= \partial_x v_x + \partial_z v_z, \\ \text{curl}(\vec{v}) &= -\partial_z v_x + \partial_x v_z \end{aligned} \quad (6)$$

The regularization functional $J_{\text{Reg}}(\vec{v})$ was defined as:

$$J_{\text{Reg}}(\vec{v}) = \int_{\Omega} \left\| \vec{\nabla} \text{div}(\vec{v}) \right\|^2 + \left\| \vec{\nabla} \text{curl}(\vec{v}) \right\|^2 \quad (7)$$

Arigovindan *et al.* [3] also used a first order regularization (*i.e.*, $\int_{\Omega} (\text{div}(\vec{v}))^2$ and $\int_{\Omega} (\text{curl}(\vec{v}))^2$) to further constraint the problem. This was not considered in our study since it tended to oversmooth the velocities. This second order regularization only enforces smoothness of the local compressions (*i.e.*, $\text{div}(\vec{v})$) and rotations (*i.e.*, $\text{curl}(\vec{v})$). The global cost function to be minimized is finally written as:

$$J(\vec{v}) = J_{\text{Data}}(\vec{v}) + \alpha J_{\text{Reg}}(\vec{v}), \quad (8)$$

where α is the regularization constant parameter. The parameter α is related to the spatial resolution, as will be described in section III.D.

4) *Robust Regularization Using Reweighted Least Squares*: We implemented an iterative reweighting least-squares method to reject local outliers that might appear due to out-of-plane motion, clutter or thermal acquisition noise. The optical-flow and Doppler weights (ω_{of} and ω_D) were initialized using the expression:

$$\omega_0 = \frac{2V_N - \sigma_D}{2V_N + \sigma_D}, \quad (9)$$

where V_N is the Nyquist Doppler velocity and σ_D the tissue Doppler standard deviation computed using (2). Since $\sigma_D \in [0, 2V_N]$, $\omega_0 \in [0, 1]$. These initial weights provided lower contribution to samples with large tissue Doppler variance. The weights were then iteratively updated using the residuals computed at the i^{th} step: $r_{\text{of}}^i = \vec{d}_{\text{of}} \cdot \vec{v}^i - v_{\text{of}}$ and $r_D^i = \vec{d}_D \cdot \vec{v}^i - v_D$. A bisquare function ($\rho(r) = \left(1 - (r/(6m))^2\right)^2$, with m being the median absolute deviation of the residuals) assigned small weights to data points with large residuals:

$$\begin{aligned}\omega_{\text{of}}^{i+1} &= \omega_0 \cdot \rho\left(r_{\text{of}}^i\right), \\ \omega_D^{i+1} &= \omega_0 \cdot \rho\left(r_D^i\right).\end{aligned}\quad (10)$$

B. Numerical Representation of the Functional

An approximate solution of the minimization problem was computed over a Cartesian grid of size $(M \times N)$ with constant axial and lateral steps (h_z and h_x). The differential operators in the cost function (6) were approximated by their discrete counterpart using three-point stencils. Using ℓ_2 -norms, the discretized problem was reduced to an unconstrained quadratic problem, as shown below. For the sake of a compact matrix formulation, we introduce the following matrices, all of size $(M \times N)$:

- V_{of} contains the optical flow velocities defined in (3).
- V_D contains the tissue Doppler velocities defined in (4).
- V_x and V_z contain the lateral and axial velocities to be estimated.
- $D_{\text{of},x}$, $D_{\text{of},z}$ contain the lateral and axial components of the unit vector \vec{d}_{of} describing the local orientation of the B-mode texture.
- $D_{D,x}$, $D_{D,z}$ contain the lateral and axial components of the unit vector describing the Doppler axis \vec{d}_D .

We also define the following column vectors of size $(MN \times 1)$ obtained by vectorizing the abovementioned matrices:

- $v_D = \text{vec}(V_D)$, $v_{\text{of}} = \text{vec}(V_{\text{of}})$, $v_x = \text{vec}(V_x)$, $v_z = \text{vec}(V_z)$, $\mathbf{d}_{D,x} = \text{vec}(D_{D,x})$, $\mathbf{d}_{D,z} = \text{vec}(D_{D,z})$, $\mathbf{d}_{\text{of},x} = \text{vec}(D_{\text{of},x})$, $\mathbf{d}_{\text{of},z} = \text{vec}(D_{\text{of},z})$.

We note I_k the identity matrix of size $(k \times k)$, \circ and \otimes the Hadamard (entrywise) and Kronecker products and $\text{diag}(\cdot)$ the diagonal matrix. The 1st-order and 2nd-order derivative operator matrices of size $(k \times k)$ are noted \dot{D}_k and \ddot{D}_k and are described in the supplementary materials. Finally, $\mathbf{v} = [v_x^T, v_z^T]^T$ is the column vector of size $(2MN \times 1)$ that corresponds to the solution of the minimization problem. Using these notations, the discretized functional to be minimized can be written as:

$$\begin{aligned}J(\mathbf{v}) &= (1-p) (\mathbf{Q}_{\text{of}}\mathbf{v} - v_{\text{of}})^T \mathbf{W}_{\text{of}}^i (\mathbf{Q}_{\text{of}}\mathbf{v} - v_{\text{of}}) \\ &+ p (\mathbf{Q}_D\mathbf{v} - v_D)^T \mathbf{W}_D^i (\mathbf{Q}_D\mathbf{v} - v_D) \\ &+ \alpha \left(\mathbf{v}^T \mathbf{Q}_{\nabla\text{div}}^T \mathbf{Q}_{\nabla\text{div}} \mathbf{v} + \mathbf{v}^T \mathbf{Q}_{\nabla\text{curl}}^T \mathbf{Q}_{\nabla\text{curl}} \mathbf{v} \right)\end{aligned}\quad (11)$$

where $\mathbf{W}_{\text{of}}^i = \text{diag}(\omega_{\text{of}}^i)$ and $\mathbf{W}_D^i = \text{diag}(\omega_D^i)$ are $(MN \times MN)$ diagonal matrices containing the optical-flow and Doppler weights (see Section III.A.3; \mathbf{Q}_D and \mathbf{Q}_{of} are two matrices of size $(MN \times 2MN)$; and $\mathbf{Q}_{\nabla\text{div}}$ and $\mathbf{Q}_{\nabla\text{curl}}$

are matrices of size $(2MN \times 2MN)$. The \mathbf{Q} matrices are given by (see the supplementary materials for details on calculation):

$$\begin{aligned}\mathbf{Q}_{\text{of}} &= \left[\text{diag}(\mathbf{d}_{\text{of},x}) \quad \text{diag}(\mathbf{d}_{\text{of},z}) \right] \\ \mathbf{Q}_D &= \left[\text{diag}(\mathbf{d}_{D,x}) \quad \text{diag}(\mathbf{d}_{D,z}) \right] \\ \mathbf{Q}_{\nabla\text{div}} &= \begin{bmatrix} \frac{1}{h_x^2} (\ddot{D}_N \otimes I_M) & \frac{1}{h_z h_x} (\dot{D}_N \otimes \dot{D}_M) \\ \frac{1}{h_z h_x} (\dot{D}_N \otimes \dot{D}_M) & \frac{1}{h_z^2} (I_N \otimes \ddot{D}_M) \end{bmatrix} \\ \mathbf{Q}_{\nabla\text{curl}} &= \begin{bmatrix} -\frac{1}{h_z h_x} (\dot{D}_N \otimes \dot{D}_M) & \frac{1}{h_x^2} (\dot{D}_N \otimes I_M) \\ -\frac{1}{h_z^2} (I_N \otimes \dot{D}_M) & \frac{1}{h_z h_x} (\dot{D}_N \otimes \dot{D}_M) \end{bmatrix}\end{aligned}\quad (12)$$

By minimizing the functional $J(\mathbf{v})$ (equations (11) and (12)), the linear system to be solved reads:

$$\mathbf{A}\mathbf{v} = \mathbf{b}$$

with:

$$\begin{aligned}\mathbf{A} &= (1-p) \mathbf{Q}_{\text{of}}^T \mathbf{W}_{\text{of}} \mathbf{Q}_{\text{of}} + p \mathbf{Q}_D^T \mathbf{W}_D \mathbf{Q}_D \\ &+ \alpha \left(\mathbf{Q}_{\nabla\text{div}}^T \mathbf{Q}_{\nabla\text{div}} + \mathbf{Q}_{\nabla\text{curl}}^T \mathbf{Q}_{\nabla\text{curl}} \right) \\ \text{and } \mathbf{b} &= (1-p) \mathbf{Q}_{\text{of}}^T \mathbf{W}_{\text{of}} v_{\text{of}} + p \mathbf{Q}_D^T \mathbf{W}_D v_D\end{aligned}\quad (13)$$

The matrix \mathbf{A} is a sparse symmetric matrix of size $(2MN \times 2MN)$, and \mathbf{b} is a column vector of size $(2MN \times 1)$.

C. Algorithm Implementation

The proposed algorithm was implemented in Matlab 7.10 (MathWorks Inc., Natick, MA, USA) on a 5-core CPU at 3.3 GHz. It consisted of 6 steps:

Step 1: Compute the optical-flow velocities and directions (V_{of} , $D_{\text{of},x}$ and $D_{\text{of},z}$, see section III.A.1), the Doppler directions ($D_{D,x}$ and $D_{D,z}$), and the initial weights ω_{of} and ω_D (Eq. 9).

Step 2: Build the vectors and matrices in (13) using (12) (see also Section I in the supplementary materials for details).

Step 3: Solve the least-squares system (13) with a Cholesky solver to obtain the velocity field.

Step 4: Update the weighting functions ω_D and ω_{of} according to the residuals (see (10) in section III.A.4).

Step 5: Repeat steps 2 to 4 to get the robust least squares solution. In practice, three iterations were sufficient to reach convergence.

To evaluate the contribution of the Doppler term in the regularization, we defined two configurations of the functional. The first one, referred to as ‘‘VVI (OF)’’ in the Result section, did not consider the Doppler term (*i.e.*, $p = 0$). The second configuration, referred to as ‘‘VVI (TDI & OF)’’ (tissue Doppler imaging with optical flow) considered equal balance between the optical flow and Doppler terms (*i.e.*, $p = 0.5$). Note that $p = 1$ leads to an ill-posed problem since Doppler velocities are only available along the radial axis.

D. Tuning the Regularization Parameters

One of the major issues in regularized methods is the setting of the regularization parameters (α in this study). Some

approaches for automatic model selection are the generalized cross-validation [32] and the L -curve [33]. In this study, we propose an alternative method. From the Plancherel theorem, the components of the regularizer (7) can be rewritten as follows:

$$\begin{aligned} \int_{\Omega} \left\| \vec{\nabla} \operatorname{div}(\vec{v}) \right\|^2 &= \int_{\Omega} \left\| \vec{\xi} \right\|^2 \left(\vec{\xi} \cdot \hat{\vec{v}} \right)^2 d\xi_x d\xi_z, \\ \int_{\Omega} \left\| \vec{\nabla} \operatorname{curl}(\vec{v}) \right\|^2 &= \int_{\Omega} \left\| \vec{\xi} \right\|^2 \left(\vec{\xi} \wedge \hat{\vec{v}} \right)^2 d\xi_x d\xi_z, \end{aligned} \quad (14)$$

with $\hat{\vec{v}}$ the spatial Fourier transform of the velocity field \vec{v} , and $\vec{\xi} = \{\xi_x, \xi_z\}$ the spatial frequencies. From (14), it is noticed that each term of the regularization functional tends to penalize high spatial frequency components of the velocity field. In this study, for sake of simplicity, equal balance was given to the curl and div terms; the regularizer thus becomes:

$$J(\vec{v}) = J_{\text{Data}}(\vec{v}) + \alpha \int_{\Omega} \left\| \vec{\xi} \right\|^4 \left\| \hat{\vec{v}} \right\|^2 d\xi_x d\xi_z \quad (15)$$

And, after defining $\alpha = (1/\xi_c)^4$, (15) yields:

$$J(\vec{v}) = J_{\text{Data}}(\vec{v}) + \int_{\Omega} \left\| \vec{\xi} / \xi_c \right\|^4 \left\| \hat{\vec{v}} \right\|^2 d\xi_x d\xi_z \quad (16)$$

When $\left| \vec{\xi} \right| \ll \xi_c$, the regularization norm is negligible with respect to the residual norm J_{Data} . This is equivalent to the conventional least-squares reconstruction (5). If $\left| \vec{\xi} \right| \gg \xi_c$, the regularization norm becomes the leading term thus forcing $\left\| \hat{\vec{v}} \right\|$ to be small. For $\left| \vec{\xi} \right| = \xi_c$, the residual norm and the velocity energy signal (*i.e.*, $\int_{\Omega} \left\| \hat{\vec{v}} \right\|^2 d\xi_x d\xi_z$) are balanced. This

is equivalent to a spatial low-pass filter with $\xi_c = 1/\sqrt[4]{\alpha}$ being its cut-off frequency. In this study, we set the cut-off frequency $\xi_c = 0.7 \text{ cm}^{-1}$ ($\approx 1/1.5 \text{ cm}$) to smooth the velocity field. When compared to regional methods (*e.g.*, 2D cross-correlation), this would correspond to the use of measurement windows of $\sim 1.5 \times 1.5 \text{ cm}$. The distance 1.5 cm matches the upper bound of the normal septal thickness at left ventricular mid-cavity.

IV. IN VITRO & IN VIVO EXPERIMENTS

Ultrasound measurements were performed with a Verasonics research scanner (V-1-128, Verasonics Inc., Redmond, WA) and a 2.5 MHz phased-array transducer (ATL P4-2, 64 elements). The raw complex envelopes (in-phase and quadrature IQ data) were sampled at 5 MHz. No apodization was introduced in transmission and reception. The IQ signals were beamformed (synthetically focused) [28], [34] using a GPU-based delay-and-sum and coherently compounded using the MoCo algorithm described in [19]. The compound data were post-scanned using linear interpolations onto a regular Cartesian grid with half-wavelength resolution (to ensure proper sampling of the spatial derivative $\vec{\nabla}$) for further processing ($h_z = h_x = 0.3 \text{ mm}$).

A. In Vitro Experiments

We tested the VVI method on a 10 cm-diameter spinning disk, as in [19]. The phantom rotated at angular velocities ranging from 1 to 4 radians per second, which gave a maximum outer speed of $\sim 20 \text{ cm/s}$. To evaluate the performance of the proposed method, we compared the estimated velocities against the ground-truth velocities of the disk. The normalized bias and normalized standard deviation were estimated as follows:

$$\begin{aligned} \text{Bias}_X &= \frac{E[X_{est} - X_{ref}]}{\max(X_{ref})}, \\ \text{Std}_X &= \sqrt{\frac{E[(X_{est} - X_{ref})^2]}{\max(X_{ref})^2} - \text{Bias}_X^2}, \end{aligned} \quad (17)$$

where X refer to the in-range or cross-range velocity, and the subscripts *ref* and *est* stand for the reference and estimated velocities, respectively. We also analyzed the effect of additive noise on velocity vector estimates at 2 rad/s (maximum outer speed of 10 cm/s): different levels of thermal white Gaussian noise were added to the raw IQ data (*i.e.*, before beamforming). The VVI algorithm was evaluated with and without the contribution of TDI (“TDI & OF”, and “OF”, *i.e.*, $p = 0.5$ and $p = 0$, respectively). We compared the global VVI algorithm with a local STE (speckle tracking) method: we used block matching on the B-mode images based on a multiscale approach of 2-D ensemble cross-correlation (2D-CC), with parabolic peak fitting [35]. We used blocks of size $3 \times 3 \text{ cm}$ and $1.5 \times 1.5 \text{ cm}$ with 90% overlap. To discard outlying vector estimates issued from 2D-CC, robust adaptive smoothing [36] was applied after each step-wise refinement.

B. In Vivo Experiments

In vivo cardiac cine-loops were acquired in five healthy volunteers. The transmit sequences were similar to those used *in vitro*. VVI sequences were obtained with both local and global methods: 1) RF-based 2D-CC (local STE), 2) B-mode-based 2D-CC (local STE), and the proposed global least-squares method, 3) with the tissue Doppler term ($p = 0.5$, “TDI&OF”), and 4) without the tissue Doppler term ($p = 0$, “OF”). Apical 3-chamber (A3C) and parasternal long axis (PSLA) views were recorded for cross-validation. These two views, related by a rigid transformation, provide the same cross-sectional plane of the myocardium, which made it possible to compare the velocity fields after spatial registration (see Figure 4 & 5). Three cardiac cycles per view (*i.e.*, A3C and PSLA) were successively acquired in the five volunteers. A total of 43 pairs were thus available for comparison (*i.e.*, A3C #1 vs. PSLA #1, 2, 3; A3C #2 vs. PSLA #1, 2, 3, *etc.*). Two acquisitions were rejected because of poor image quality. A3C and PSLA views were spatially registered using anatomical landmarks. A trained sonographer selected four markers (two in the inferolateral wall, and two in the anteroseptal wall) in each acquisition, as shown in Figure 4. The rigid transformation matrices were deduced by matching the morphological markers from one view to the other.

1) *In Vivo Cross-Validation; A3C Vs. PSLA*: To validate the proposed method, we extracted the time-resolved velocity vectors (from B-mode-based 2D-CC and TDI&OF) at the basal anteroseptal and inferolateral locations in both A3C and PSLA views (see Figure 5 & 6). To validate the in-range velocity components, the velocity vectors computed in the A3C view were projected on the Doppler axis (*i.e.*, $v_{\text{in-range}}^{\text{A3C}} = \vec{v}_{\text{2D-CC or TDI\&OF}}^{\text{A3C}} \cdot \vec{d}_D^{\text{A3C}}$) and compared with the tissue Doppler velocities (*i.e.*, v_D^{A3C}) computed from Eq. (1). To validate the cross-range velocities, we projected the PSLA velocity vectors onto the A3C Doppler axis (*i.e.*, $v_{\text{cross-range}}^{\text{PSLA}} = \vec{v}_{\text{2D-CC or TDI\&OF}}^{\text{PSLA}} \cdot \vec{d}_D^{\text{A3C}}$) and compared them with the tissue Doppler velocity (*i.e.*, v_D^{A3C}). A3C TDI was chosen as the reference since basal velocities are mostly oriented in the in-range direction (*i.e.*, the Doppler axis) in this view. Dynamic time warping was applied to account for the possible variations of the cardiac period over successive acquisitions. Correlation and agreement between in-range (TDI) and projected velocities were analyzed by linear regression (see Figure 6 and table 1). These comparisons were carried out within the myocardium; the latter was detected automatically, as explained below.

2) *Automatic Detection of the Myocardium*: As the myocardium returns strong signals and is moving coherently over time, tissue Doppler variance defined by (2) was expected to be smallest in myocardial regions. We detected the myocardium automatically by using Eq. (9). Samples with low tissue Doppler variance (*i.e.*, $\omega_0 > 0.5$) were labeled as myocardial tissues, while pixels with large variance (*i.e.*, $\omega_0 < 0.5$) were labeled as background. This strategy was also used to generate myocardial vector plots (see Figure 4).

3) *Additional Visual Evaluations*: We computed the pulse wave Doppler signal (PWD) from the compound IQ data using the following expression:

$$\text{PWD}(v, t_0) = \left| \int_{t_0}^{t_0+T} \tilde{s}_t \cdot e^{-j \frac{4\pi \cdot f_0 \cdot v}{c} t} \cdot H(t - t_0 + T/2) dt \right|^2, \quad (18)$$

where \tilde{s}_t is the complex envelope at time t and $H(\cdot)$ is a Hanning window of length $T = 65$ ms (*i.e.*, 32 time samples). Standard apical 4- chamber, 3- chamber and medial short-axis views were also recorded for visual purposes only (see Figure 7). The *in vivo* protocol was approved by the human ethical review committee of the University of Montreal Hospital Research Center.

V. RESULTS

A. In Vitro Experiments

Figure 2 shows the *in vitro* performance of the VVI regularized least-squares method, with or without including tissue Doppler imaging (*i.e.*, TDI&OF and OF, respectively). The proposed VVI method outperformed B-mode STE (*i.e.*, 2D-CC) both in terms of in-range velocity (*i.e.*, along the beam axis) and cross-range velocity (*i.e.*, perpendicular to the beam axis), even if TDI was not incorporated. Without TDI components (when $p = 0$), the proposed method lost precision and accuracy in the in-range direction (Fig. 2, left column,

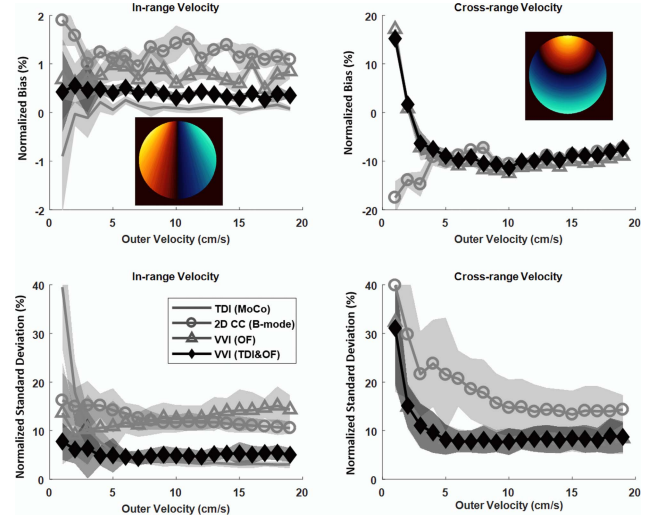


Fig. 2. *Comparison of the VVI algorithms*. Bias and standard deviation of the in-range and cross-range components (*in vitro* experiments). Block matching (circles) was compared with MoCo-based TDI (gray line) and the proposed least-squares method, with (diamonds) and without (triangles) TDI constraint. The insets represent the in-range (top left) and cross-range (top right) reference velocities. The shaded areas represent \pm one standard deviation of the estimate computed from 10 independent measures.

triangles vs. diamonds). The introduction of the TDI constraint in the functional ($p = 0.5$) had no impact on the cross-range components (Fig. 2, right column, triangles vs. diamonds).

All methods (*i.e.*, VVI OF, TDI&OF and 2D-CC) had an almost constant bias of -10% in the cross-range direction. The proposed VVI method was the most precise (standard deviation $< 10\%$) in the cross-range direction.

Overall, the proposed method (VVI TDI&OF) provided the most precise and accurate velocity vector estimates in the in-range direction, with an average bias of 0.4% and standard deviation of 5.2% . Without the TDI constraint ($p = 0$), the average bias and standard deviation increased to 0.8% and 13% respectively. In the cross-range-direction, both methods (*i.e.*, 2D-CC and TDI&OF) had an almost constant bias of $\sim 10\%$. The proposed VVI method, however, provided the most precise measurement (standard deviation: 10% vs. 18%). Adding the tissue Doppler constraint in the system did not improve the precision in the cross-range direction.

The effect of additive thermal noise became insignificant beyond a signal-to-noise ratio (SNR) of 15 dB (Fig. 3). Below 15 dB, the motion compensation algorithm described in [19] became less efficient (see [19, Fig. 9]) and altered both compound IQ and tissue Doppler quality, which in turn affected the velocity vector estimates. In general, the dual approach (*i.e.*, VVI (TDI & OF)) returned the most robust and accurate velocity fields. Whatever the method, the cross-range components were more sensitive to noise than the in-range components. Again, there was no significant difference between VVI (OF) and VVI (TDI&OF) in the cross-range direction.

B. In Vivo Cross-Validation

Figure 4 shows tissue velocity vector fields successively acquired in parasternal long axis view and apical 3-chamber

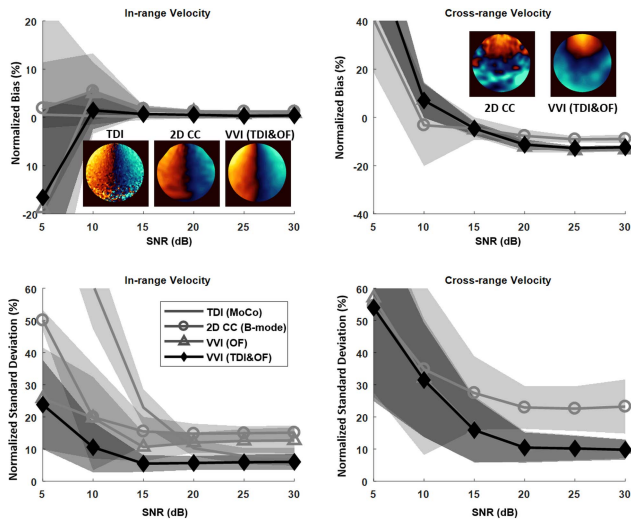


Fig. 3. Effect of noise on velocity vector estimates. Effect of SNR on bias (top panels) and standard deviation (bottom panels) for the in-range (leftmost panels) and cross-range (rightmost panels) components: same data as in Figure 2 at 2 rad/s. The insets (top row) illustrate the effect of low SNR (15 dB). Shaded areas represent \pm one standard deviation of the estimate computed from 10 independent measures.

view. When compared to one another, the velocity vector fields were consistent (see also the movie in the supplementary materials). This was particularly true during atrial contraction (a' wave) and peak systole (S' wave).

Figure 5 shows examples of basal velocities (anteroseptal and inferolateral) estimated in A3C (thick lines) and PSLA views (dashed lines), averaged over three cardiac cycles and compared to pulse-wave Doppler (PWD, white spectrogram). The in-range components estimated by VVI (TDI&OF) were highly consistent with A3C PWD. This was expected since the proposed method uses TDI as a prior to increase in-range accuracy. The cross-range components estimated in PSLA views were also highly consistent with A3C PWD, unlike 2D-CC that indicated lower reproducibility (see dashed green lines and shaded area). These results confirm the ability of the proposed method to evaluate cross-range velocity components.

Figure 6 shows the comparison between the TDI measurements in apical 3-chamber views (A3C) and their counterparts estimated from VVI (TDI&OF) or 2D-CC, either in A3C (in-range component, parallel to the beam axis) or in PSLA (cross-range component, perpendicular to the beam axis). Table 1 lists the correlations and agreements between VVI, 2D-CC and TDI.

A high correlation and a good agreement were observed between TDI and the in-range VVI component (TDI A3C vs. VVI A3C) at both locations (*i.e.*, anteroseptal and inferolateral), which confirms the performance of the proposed method in measuring in-range velocities. Without considering the TDI constraint in the functional (*i.e.*, $p = 0$), there was a slightly lower correlation and agreement. A lower correlation and agreement was observed with the 2D CC STE method (see Figure 6 and Table 1). When considering the parasternal view (PSLA), good correlation and agreement were observed with A3C TDI for the two basal locations. This confirms the ability of the proposed method to provide accurate cross-range

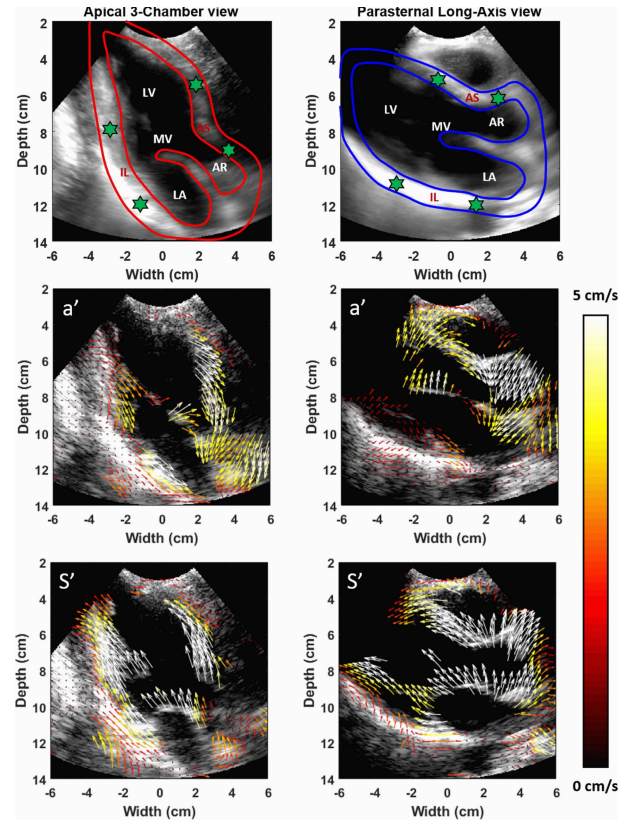


Fig. 4. In vivo high-frame-rate velocity vector imaging. These snapshots display VVI images at peak a' -wave (peak atrial contraction in second row) and S' -wave (peak systole in third row). The apical-3-chamber and parasternal-long-axis views represent the same cardiac plane from different viewpoints (first row). The two views were spatially registered using anatomical markers (green stars).

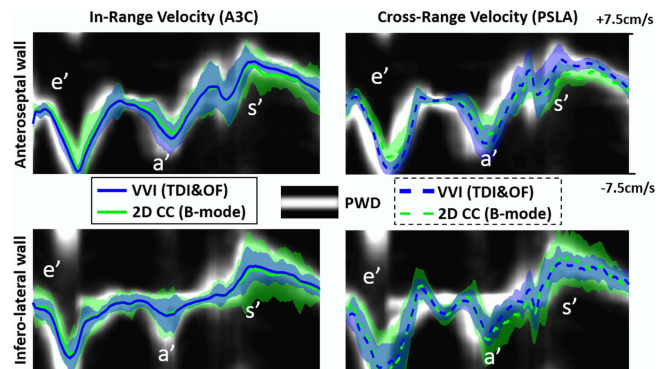


Fig. 5. In-vivo cross-validation of basal velocities. The spectrograms represent the anteroseptal and infero-lateral velocities measured by pulse-wave Doppler (from the A3C view). The VVI (TDI&OF) and 2D-CC velocities were determined from the A3C (solid curves) and PSLA (dashed curves) views. S' -wave: peak systole; e' -wave: peak ventricular relaxation; a' -wave: peak atrial contraction.

velocity measurements. As with the *in vitro* study, the TDI constraint had no impact on the cross-range precision. Lower correlation and agreement were observed with the 2D CC STE method.

Overall, the cross-range performance of both VVI and 2D CC STE were lower for the infero-lateral wall. Using the beamformed RF signals rather than the B-mode images in 2D CC STE did not improve the performance of speckle tracking.

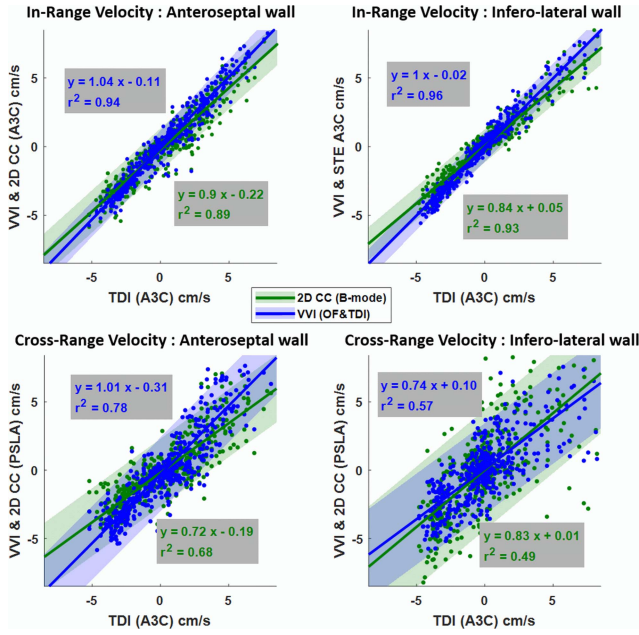


Fig. 6. Basal velocities: comparison with A3C TDI. The basal anteroseptal and infero-lateral velocities of 5 healthy volunteers were measured by high-frame rate TDI (tissue Doppler imaging) in apical 3-chamber views (A3C). They were also determined by the proposed velocity vector imaging method (VVI) and by 2D speckle tracking echocardiography (2D-CC) in: 1) A3C views (first row), to evaluate the in-range accuracy and 2) PSLA views (second row), to evaluate the cross-range accuracy.

TABLE I

In-vivo CORRELATION AND AGREEMENT BETWEEN VVI (OF AND TDI&OF), STE (2D-CC ON B-MODE AND RF) AND A3C TISSUE DOPPLER IMAGING (TDI A3C). THE IN-RANGE VELOCITY COMPONENTS COMPUTED IN A3C WERE COMPARED WITH TDI TO STUDY IN-RANGE ACCURACY. THE CROSS-RANGE COMPONENTS COMPUTED IN PLSA WERE COMPARED WITH A3C TDI TO STUDY CROSS-RANGE ACCURACY (SAME DATA AS IN FIGURE 6)

TDI A3C vs.	In-range (A3C)					
	Anteroseptal			Inferolateral		
	slope	intercept	r^2	slope	intercept	r^2
2D CC (RF)	1.05	-0.32	0.75	0.84	0.03	0.52
2D CC (B-mode)	0.9	-0.22	0.89	0.84	0.05	0.93
VVI (OF)	1.15	-0.22	0.92	1.06	0.01	0.91
VVI (OF&TDI)	1.04	-0.11	0.94	1	-0.02	0.96

TDI A3C vs.	Cross-range (PSLA)					
	Anteroseptal			Inferolateral		
	slope	intercept	r^2	slope	intercept	r^2
2D CC (RF)	0.8	-0.27	0.25	0.64	0	0.17
2D CC (B-mode)	0.72	-0.19	0.68	0.83	0.01	0.49
VVI (OF)	1.04	-0.26	0.76	0.75	0.15	0.57
VVI (OF&TDI)	1.01	-0.31	0.78	0.74	0.1	0.57

Figure 7 finally shows velocity vector images, estimated with the proposed VVI method (TDI&OF) and overlaid on the high-frame-rate B-mode images, for the medial short axis, apical 2-chamber and apical 4-chamber views of one volunteer.

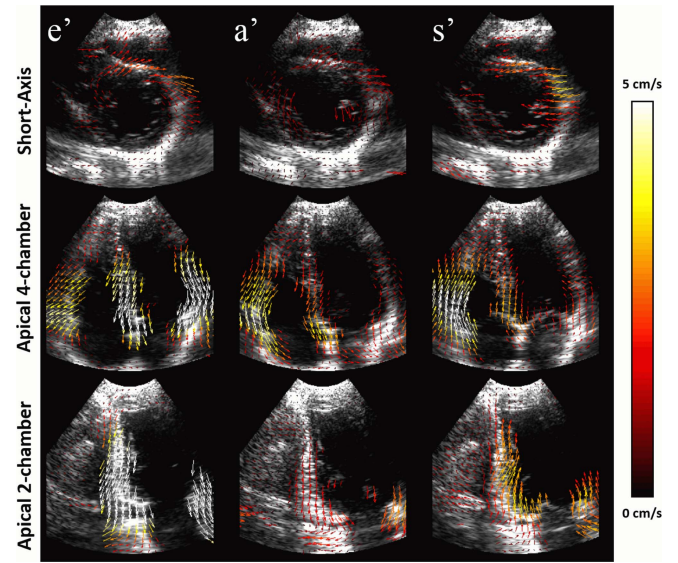


Fig. 7. High-frame rate velocity vector images. Medial short-axis, apical 4-chamber and apical 2-chamber views of high-frame-rate B-mode + velocity vector echocardiographic images. e'-wave: left ventricular relaxation, a'-wave: atrial contraction and S'-wave: peak systole.

During left ventricular relaxation (e'-wave), one can notice the downward motion of the septum and lateral walls (*i.e.*, away from the apex) in the apical 4-chamber view. Left ventricular untwisting is visible in the medial short-axis view. Opposite motions are visible during systole (S'-wave).

VI. DISCUSSION

In this paper, we presented an original global framework for high-frame-rate velocity vector imaging. We used tilted circular diverging beams with motion compensation, as proposed in our previous study [19], to produce wide-sector (*i.e.*, 90°) high-resolution B-mode and tissue Doppler images at 500 FPS. To overcome the inability of tissue Doppler imaging to provide 2D velocity estimates and to optimize the performance of speckle tracking methods, the main contribution of this work was to combine high-frame-rate tissue Doppler and B-mode optical flow within a dedicated regularized least-squares method.

A. Quality of the Reconstructed Vector Velocity Field

The effectiveness of the proposed dual method was demonstrated *in vitro*. It was observed that the Doppler term had a positive impact on the in-range velocity estimation (see Figure 2), and for high level of noise (see Figure 3). Indeed, Doppler velocities extracted from the motion compensation algorithm [19] were computed over large ensembles (*i.e.*, 36 transmits) and with an effective PRF of 4500 Hz, thus providing a low-variance estimate of the in-range velocity (Doppler variance decreases as the ensemble length increases [37]) with a wide range of admissible velocities ($V_N \approx 35$ cm/s). Despite the limited lateral resolution of transthoracic echocardiography associated with the limited footprint of phased array transducers, the proposed method provided accurate velocity estimates in the cross-range direction. The Doppler constraint, however, did not impact the

cross-range components (see black diamonds vs. gray triangles in Fig. 2). Overall, the proposed method outperformed the 2D cross-correlation STE method, likely because of the combination of B-mode optical flow, tissue Doppler and the robust vector regularization.

The superiority of the proposed VVI method over 2D cross-correlation STE was also demonstrated *in vivo* with a cross-validation strategy (see Figure 4, 5, 6 and table 1). In-range (i.e., parallel to the beam axis) and cross-range (i.e., perpendicular to the beam axis) velocities were consistent with the reference tissue Doppler (TDI), especially for the basal antero-septal location which is closer to the probe. Basal infero-lateral velocities showed lower correlation with the reference TDI than the antero-septal one. This may be attributed to the lower cross-range resolution of B-mode at larger depth. Note that the basal lateral location is also more subject to clutter noise since it is closer to the pericardium, which tends to produce strong echoes (see Figure 4). It may also be subject to aliasing and broadening. Indeed, we noticed aliased frequencies and spectral broadening in the spectrogram of the basal lateral velocity in A3C (see Figure 5 at e' and S' waves). STE seemed more sensitive to aliasing and broadening than the proposed VVI approach. Because VVI uses unaliased tissue Doppler ($V_N \approx 35$ cm/s) as a prior knowledge of the in-range velocity, it may be less sensitive to such artefact. Such discrepancies may also be attributed to misalignment between A3C and PSLA views during cross-validation. Overall, the proposed method outperformed STE both *in vitro* and *in vivo* and could be considered as a robust method for VVI.

B. Expected Clinical Significance and In Vivo Reproducibility

Recovering multidimensional tissue velocity vector may provide new diagnostic information to evaluate myocardial regional function. A recent clinical study [4] demonstrated the ability of 2D speckle tracking methods to evaluate cardiac strains in all four cardiac chambers, at rest, using conventional echocardiographic systems. In the context of stress echocardiography, such methods might fail due to the larger inter-frame decorrelation associated with the limited frame rate (~ 50 FPS in [4]). In this study, we developed a regularization framework based on ultrafast duplex echocardiography (i.e., B-mode and TDI) [19] to evaluate tissue velocity vector dynamics at 500 FPS. The clinical relevance of the proposed method in the context of stress echocardiography remains to be confirmed. If it does, to become an accepted echocardiographic procedure, this method must be fast and reproducible. Fastness is ensured since it only requires one series of ultrafast acquisitions [19]. Furthermore, in the proposed sparse configuration, the nonzero elements of the matrix A are located around the diagonal (see supplementary materials for details). The solution can thus be obtained by solving a sparse symmetric, well-conditioned and diagonally dominant linear system of equations. Computationally efficient methods exist to solve such a system.

To guarantee inter-observer reproducibility, the choice of the regularization parameter must be objective. In other regularization frameworks [3], [38], the choice of the regularization

parameter was left to the user or evaluated empirically. In this study, we gave physical meaning (i.e., cutoff frequency of a spatial low pass filter; see Section III.D) to the regularization parameters thus allowing controlling the spatial resolution of the output velocity field.

C. Limitations and Potential Improvements

The proposed algorithm was validated *in vitro* and *in vivo*. Although *in vivo* results seemed promising, several limitations deserve to be pointed out:

- The main issue associated with ultrafast echocardiography, especially using tissue Doppler imaging, is the impact of clutter noise. Clutter arises from hyperechoic neighboring structures whose velocity differs from the actual local velocity to be estimated. Doppler signals thus display multiple frequencies (i.e., broadening), aside from the main shifted one, which may alter velocity estimation and motion compensation [17], [19]. The proposed method may be sensitive to clutter. In this study, to address the problem of clutter noise, we proposed the use of reweighted least squares (see Section III.A.4). This method would need further evaluation in strong clutter environments (e.g. calcified valve leaflets).
- The velocity vector field retrieved by the proposed method approximates the actual velocity as it only considers the in-plane 2D motions. B-mode optical flow remains sensitive to out-of-plane motions since it creates local intensity variations unrelated with the in-plane motion. In this study, its combination with tissue Doppler imaging, which is not sensitive to intensity variations [10], [11], makes it potentially more robust than conventional optical flow methods. An effective way to address this issue would be to perform 3D velocity vector reconstruction using 3D echocardiographic sequences, as discussed in the following section.
- Speckle tracking can be performed on beamformed RF data rather than B-mode envelope. This methodology may provide a better precision on the radial velocities owing to the high frequency contents in the RF data. However, there is no evidence, in the literature, that this approach provides a better estimate of the cross-range velocities. We found that using RF data rather than B-mode images (see Table 1) had a negative impact on the effectiveness of 2D speckle tracking. Note that we reconstructed RF data from motion-compensated IQ data; they might be subject to motion artefacts and thus RF decorrelation. In this study, to increase performance in the radial direction without dealing with RF data, we used high-frame rate tissue Doppler imaging.
- Harmonic imaging has become the default mode in echocardiography because of its beneficial impact on clutter mitigation. Harmonic imaging, however, is little compatible with diverging wave imaging. Harmonic imaging relies on non-linear propagation phenomena that require higher intensities. A possible approach could be pulse inversion. Correia *et al.* [39] have recently illustrated the feasibility of harmonic echocardiography

with diverging beams through pulse inversions. We could possibly combine pulse inversion with MoCo to increase the contrast in B-mode echocardiography, and in turn improve VVI accuracy using the proposed framework.

D. Three-Dimensional Velocity Vector Imaging

The velocity vector imaging method described in this study could be extended to 3-D echocardiography. To this end, the functional described in Section III-D must be rewritten using the three velocity components. The optical flow would benefit from such a 3-D representation since it would no longer be subject to intensity variations associated with out-of-plane motions. High-frame-rate echocardiography using diverging waves has recently been proposed in 3-D [40]. A similar motion compensation sequence could be designed for 3-D cardiac imaging and would benefit from MoCo as numerous transmissions are needed to increase image quality [17], [19], [24]. Furthermore, a divergence-free constraint, specific to incompressible tissue materials, could be included in the regularizer. Note that this constraint could not be considered in this study because of the incompleteness of the divergence operator in 2-D. The method could finally be extended to 2-D + t and 3-D + t by considering additional regularization constraints related to tissue accelerations or strain rates. One could also consider the periodic motion of the myocardium, as in [38], to further constraint the problem by using multiple successive cardiac cycles.

VII. CONCLUSION

We demonstrated the feasibility of recovering 2D velocity vector fields from motion compensated high-frame-rate B-mode echocardiography using a global optical flow and tissue Doppler method. The proposed minimization framework provided an efficient solution to the velocity vector imaging problem. The benefit of adding tissue Doppler constraints was also illustrated. Further developments may include the derivation of regional strains for the assessment of myocardial contractility.

REFERENCES

- [1] S. F. Nagueh *et al.*, "Recommendations for the evaluation of left ventricular diastolic function by echocardiography: An update from the American Society of Echocardiography and the European Association of Cardiovascular Imaging," *J. Amer. Soc. Echocardiogr.*, vol. 29, no. 4, pp. 277–314, Apr. 2016.
- [2] J. D'Hooge, "Regional strain and strain rate measurements by cardiac ultrasound: Principles, implementation and limitations," *Eur. Heart J.-Cardiovascular Imag.*, vol. 1, no. 3, pp. 154–170, 2000.
- [3] M. Arigovindan, M. Suhling, C. Jansen, P. Hunziker, and M. Unser, "Full motion and flow field recovery from echo Doppler data," *IEEE Trans. Med. Imag.*, vol. 26, no. 1, pp. 31–45, Jan. 2007.
- [4] K. Addetia *et al.*, "Simultaneous longitudinal strain in all 4 cardiac chambers: A novel method for comprehensive functional assessment of the heart," *Circulat., Cardiovascular Imag.*, vol. 9, no. 3, p. e003895, 2016.
- [5] P. Reant *et al.*, "Experimental validation of circumferential, longitudinal, and radial 2-Dimensional strain during dobutamine stress echocardiography in ischemic conditions," *J. Amer. College Cardiol.*, vol. 51, no. 2, pp. 149–157, 2008.
- [6] M. Sühling *et al.*, "Multiscale motion mapping: A novel computer vision technique for quantitative, objective echocardiographic motion measurement independent of Doppler: first clinical description and validation," *Circulation*, vol. 110, no. 19, pp. 3093–3099, 2004.
- [7] M. Suhling, M. Arigovindan, C. Jansen, P. Hunziker, and M. Unser, "Myocardial motion analysis from B-mode echocardiograms," *IEEE Trans. Image Process.*, vol. 14, no. 4, pp. 525–536, Apr. 2005.
- [8] A. R. Porras *et al.*, "Improved myocardial motion estimation combining tissue Doppler and B-mode echocardiographic images," *IEEE Trans. Med. Imag.*, vol. 33, no. 11, pp. 2098–2106, Nov. 2014.
- [9] V. Tavakoli, N. Bhatia, R. A. Longaker, M. F. Stoddard, and A. A. Amini, "Tissue Doppler imaging optical flow (TDIOF): A combined B-mode and tissue Doppler approach for cardiac motion estimation in echocardiographic images," *IEEE Trans. Biomed. Eng.*, vol. 61, no. 8, pp. 2264–2277, Aug. 2014.
- [10] D. J. Fleet and A. D. Jepson, "Computation of component image velocity from local phase information," *Int. J. Comput. Vis.*, vol. 5, no. 1, pp. 77–104, 1990.
- [11] D. Fleet and Y. Weiss, "Optical flow estimation," in *Handbook of Mathematical Models in Computer Vision*. New York, NY, USA: Springer, 2006, pp. 237–257.
- [12] L. Tong, A. Ramalli, R. Jasaityte, P. Tortoli, and J. D'Hooge, "Multi-transmit beamforming for fast cardiac imaging-experimental validation and *in vivo* application," *IEEE Trans. Med. Imag.*, vol. 33, no. 6, pp. 1205–1219, Jun. 2014.
- [13] L. Tong *et al.*, "Wide-angle tissue Doppler imaging at high frame rate using multi-line transmit beamforming: An experimental validation *in vivo*," *IEEE Trans. Med. Imag.*, vol. 35, no. 2, pp. 521–528, Feb. 2016.
- [14] J. A. Jensen, S. I. Nikolov, K. L. Gammelmark, and M. H. Pedersen, "Synthetic aperture ultrasound imaging," *Ultrasonics*, vol. 44, pp. 5–15, Dec. 2006.
- [15] G. Montaldo, M. Tanter, J. Bercoff, N. Benech, and M. Fink, "Coherent plane-wave compounding for very high frame rate ultrasonography and transient elastography," *IEEE Trans. Ultrason., Ferroelect., Freq. Control*, vol. 56, no. 3, pp. 489–506, Mar. 2009.
- [16] J.-Y. Lu, "2D and 3D high frame rate imaging with limited diffraction beams," *IEEE Trans. Ultrason., Ferroelect., Freq. Control*, vol. 44, no. 4, pp. 839–856, Jul. 1997.
- [17] B. Denarie *et al.*, "Coherent plane wave compounding for very high frame rate ultrasonography of rapidly moving targets," *IEEE Trans. Med. Imag.*, vol. 32, no. 7, pp. 1265–1276, Jul. 2013.
- [18] L. Tong, H. Gao, H. Choi, and J. D'Hooge, "Comparison of conventional parallel beamforming with plane wave and diverging wave imaging for cardiac applications: A simulation study," *IEEE Trans. Ultrason., Ferroelect., Freq. Control*, vol. 59, no. 8, pp. 1654–1663, Aug. 2012.
- [19] J. Porée, D. Posada, A. Hodzic, F. Tourmoux, G. Cloutier, and D. Garcia, "High-frame-rate echocardiography using coherent compounding with Doppler-based motion-compensation," *IEEE Trans. Med. Imag.*, vol. 35, no. 7, pp. 1647–1657, Jul. 2016.
- [20] D. Posada *et al.*, "Staggered multiple-PRF ultrafast color Doppler," *IEEE Trans. Med. Imag.*, vol. 35, no. 6, pp. 1510–1521, Jun. 2016.
- [21] H. Hasegawa and H. Kanai, "High-frame-rate echocardiography using diverging transmit beams and parallel receive beamforming," *J. Med. Ultrason.*, vol. 38, no. 3, pp. 129–140, 2011.
- [22] C. Papadacci, M. Pernot, M. Couade, M. Fink, and M. Tanter, "High-contrast ultrafast imaging of the heart," *IEEE Trans. Ultrason., Ferroelect., Freq. Control*, vol. 61, no. 2, pp. 288–301, Feb. 2014.
- [23] D. P. Shattuck, M. D. Weinschenker, S. W. Smith, and O. T. von Ramm, "Explosocan: A parallel processing technique for high speed ultrasound imaging with linear phased arrays," *J. Acoust. Soc. Amer.*, vol. 75, no. 4, pp. 1273–1282, 1984.
- [24] K. L. Gammelmark and J. A. Jensen, "2-D tissue motion compensation of synthetic transmit aperture images," *IEEE Trans. Ultrason., Ferroelect., Freq. Control*, vol. 61, no. 4, pp. 594–610, Apr. 2014.
- [25] K. S. Kim, J. S. Hwang, J. S. Jeong, and T. K. Song, "An efficient motion estimation and compensation method for ultrasound synthetic aperture imaging," *Ultrason. Imag.*, vol. 24, no. 2, pp. 81–99, 2002.
- [26] G. E. Trahey and L. P. Nock, "Synthetic receive aperture imaging with phase correction for motion and for tissue inhomogeneities. II. Effects of and correction for motion," *IEEE Trans. Ultrason., Ferroelect., Freq. Control*, vol. 39, no. 4, pp. 496–501, Jul. 1992.
- [27] A. R. Porras *et al.*, "Myocardial motion estimation combining tissue Doppler and B-mode echocardiographic images," in *Proc. Int. Conf. Med. Image Comput. Comput.-Assisted Intervent.*, 2013, pp. 484–491.
- [28] D. C. M. Horvat, J. S. Bird, and M. M. Goulding, "True time-delay bandpass beamforming," *IEEE J. Ocean. Eng.*, vol. 17, no. 2, pp. 185–192, Apr. 1992.
- [29] B. K. P. Horn and B. G. Schunck, "Determining optical flow," *Artif. Intell.*, vol. 17, nos. 1–3, pp. 185–203, Aug. 1981.

- [30] L. Le Tarnec, F. Destrempes, G. Cloutier, and D. Garcia, "A proof of convergence of the Horn-Schunck optical flow algorithm in arbitrary dimension," *SIAM J. Imag. Sci.*, vol. 7, no. 1, pp. 277–293, 2014.
- [31] T. Corpetti, E. Memin, and P. Perez, "Dense estimation of fluid flows," *IEEE Trans. Pattern Anal. Mach. Intell.*, vol. 24, no. 3, pp. 365–380, Mar. 2002.
- [32] D. Garcia, "Robust smoothing of gridded data in one and higher dimensions with missing values," *Comput. Statist. Data Anal.*, vol. 54, no. 4, pp. 1167–1178, Apr. 2010.
- [33] P. C. Hansen and D. P. O'Leary, "The use of the L-curve in the regularization of discrete III-posed problems," *SIAM J. Sci. Comput.*, vol. 14, no. 6, pp. 1487–1503, 1993.
- [34] K. Ranganathan, M. K. Santy, T. N. Blalock, J. A. Hossack, and W. F. Walker, "Direct sampled I/Q beamforming for compact and very low-cost ultrasound imaging," *IEEE Trans. Ultrason., Ferroelect., Freq. Control*, vol. 51, no. 9, pp. 1082–1094, Sep. 2004.
- [35] C. D. Meinhart, S. T. Wereley, and J. G. Santiago, "A PIV algorithm for estimating time-averaged velocity fields," *J. Fluids Eng.*, vol. 122, no. 2, pp. 285–289, 2000.
- [36] D. Garcia, "A fast all-in-one method for automated post-processing of PIV data," *Experim. Fluids*, vol. 50, no. 5, pp. 1247–1259, Oct. 2010.
- [37] D. H. Evans and W. N. McDicken, *Doppler Ultrasound: Physics, Instrumentation and Signal Processing*. Hoboken, NJ, USA: Wiley, 2000.
- [38] A. Gomez *et al.*, "4D blood flow reconstruction over the entire ventricle from wall motion and blood velocity derived from ultrasound data," *IEEE Trans. Med. Imag.*, vol. 34, no. 11, pp. 2298–2308, Nov. 2015.
- [39] M. Correia, J. Provost, S. Chatelin, O. Villemain, M. Tanter, and M. Pernot, "Ultrafast harmonic coherent compound (UHCC) imaging for high frame rate echocardiography and shear-wave elastography," *IEEE Trans. Ultrason., Ferroelect., Freq. Control*, vol. 63, no. 3, pp. 420–431, Mar. 2016.
- [40] J. Provost *et al.*, "3D ultrafast ultrasound imaging *in vivo*," *Phys. Med. Biol.*, vol. 59, no. 19, pp. L1–L13, 2014.
- [41] M. V. Andersen *et al.*, "High-frame-rate deformation imaging in two dimensions using continuous speckle-feature tracking," *Ultrasound Med. Biol.*, vol. 42, no. 11, pp. 2606–2615, 2016.